Journal of Hazardous Materials 500 (2025) 140317

Contents lists available at ScienceDirect

Journal of Hazardous Materials

journal homepage: www.elsevier.com/locate/jhazmat

Engineering microbiome for carbonate precipitation in heavy oil produced water: Hot-zone identification of ion accumulation and crystallization

Jianhua Lei [a,b], Shuhui Zhang [a,b], Chuanfu Zhao [a,b], Lei Zhang [c], Yuke Li [d], Weizhi Zhou [a,b,*]

[a] School of Civil Engineering, Shandong University, Jinan, Shandong 250000, PR China
[b] Laboratory of water-sediment regulation and eco-decontamination, Jinan, Shandong 250000, PR China
[c] Sinopec Petroleum Engineering Design Co., Ltd, Dongying, Shandong 257026, PR China.
[d] Department of Water Management, Faculty of Civil Engineering and Geosciences, Delft University of Technology, Stevinweg 1, Delft 2628 CN, the Netherlands

HIGHLIGHTS

- Engineering microbiome achieved continuous precipitation of hardness ions.
- The −OH group of EPS is the ion accumulation hot zone in neutrality condition.
- The $-COO^-$ is the carbonate crystallization site under alkaline condition.
- The initial growth of amorphous carbonate is confined to intracellular compartment.
- Urease-positive and hydrocarbon-degrading bacteria dominate the microbiome.

GRAPHICAL ABSTRACT

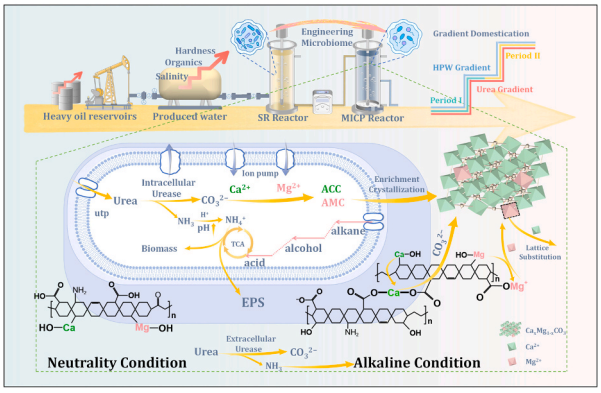

ARTICLE INFO

Keywords:
Biomineralization
Calcium
Engineering microbiome
Extracellular polymeric substances
Heavy oil produced water

ABSTRACT

Microbially induced carbonate precipitation (MICP) presents a promising strategy for the softening and purification of produced water. However, produced water from heavy oil reservoirs exhibits high salinity, refractory organics, particularly with hardness ions such as Ca^{2+} and Mg^{2+}, all of which substantially inhibit microbial mineralization activity. Industrially viable continuous-flow operational strategies remain underdeveloped, and the underlying biomineralization mechanisms are not yet fully elucidated. Here, we report the successful construction of an engineering microbiome through substrate gradient acclimation, achieving continuous and stable precipitation of Ca^{2+} (87.28 %) and Mg^{2+} (84.16 %). The process also revealed the sequential transformation of organic functional groups under high salinity perturbation. Hydroxyl groups (−OH) in extracellular polymeric substances preferentially bound divalent cations under neutral conditions, whereas carboxyl groups ($-COO^-$) served as nucleation sites for carbonate formation under alkaline conditions. Extracellular carbonate precipitation predominated, while a minor fraction of amorphous magnesium carbonate was accumulated intracellularly. The engineering microbiome, dominated by urease-positive and hydrocarbon-degrading taxa, tolerated extreme salinity and hardness through metabolic complementarity and coordinated gene regulation. These findings

* Corresponding author at: School of Civil Engineering, Shandong University, Jinan, Shandong 250000, PR China.
E-mail address: wzzhou@sdu.edu.cn (W. Zhou).

https://doi.org/10.1016/j.jhazmat.2025.140317
Received 22 August 2025; Received in revised form 15 October 2025; Accepted 29 October 2025
Available online 31 October 2025

demonstrate a robust, continuous-flow MICP process for HPW treatment, offering a foundation for industrial-scale integration with improved stability, efficiency, and microbiome resilience in complex environments.

1. Introduction

The accelerated exploitation of heavy oil resources has intensified the generation of hypersaline produced water (PW), posing substantial environmental and operational challenges [1,2]. Compared to conventional PW, heavy oil produced water (HPW) is characterized by extreme ionic concentrations and complex organic matrices, primarily resulting from high-temperature extraction techniques such as steam-assisted gravity drainage [3–6]. This geochemical process elevates ionic concentrations in HPW to extremes of 6200–40000 mg/L Ca^{2+} and 570–3700 mg/L Mg^{2+}, as quantified in Marcellus Shale Gas PW [7]. Such conditions severely hinder water reuse complicate valuable metal recovery, and magnify the environmental footprint of heavy oil production [8–10]. Although advanced desalination technologies such as multi-effect distillation, electrodialysis, and bioelectrochemical systems each offer specific advantages in terms of energy efficiency or functional integration [11–15], they remain insufficient for HPW treatment. Their performance is constrained by high energy demand, membrane fouling, limited reaction efficiency, and operational complexity.

Against this backdrop, the pursuit for innovative, low-footprint solutions had intensified, steering scientific inquiry toward bio-inspired strategies that harmonized industrial needs with planetary boundaries. In particular, microbially induced carbonate precipitation (MICP) has emerged as a promising bio-mediated process capable of immobilizing hardness ions through microbially driven carbonate formation [16,17]. MICP is a rapid process that utilizes bacterial urease to hydrolyze urea, producing carbonate and ammonia; the subsequent pH elevation promotes carbonate mineral precipitation [18]. Initially developed for geotechnical reinforcement, MICP has evolved into a versatile platform for environmental remediation [19]. Numerous studies have demonstrated its potential for PW treatment. For instance, *Staphylococcus succinus* effectively removed Ca^{2+}, organic contaminants, and heavy metals including As, Mn, and Cu from PW under low-nutrient conditions [20]. The magnesium ammonium phosphate enhanced *Sporosarcina pasteurii* based MICP process converts lead and cadmium into more stable forms [21], whereas microplastics were found to inhibit ureolytic bacteria–based Cd remediation [22]. Additionally, free and immobilized *Lysinibacillus fusiformis* precipitated Ca^{2+} and Mg^{2+} as calcium carbonate and struvite, respectively. Hu et al. pioneered the use of MICP for PW softening by integrating ureolytic bacterial consortia with biochar-enhanced biofilters [16].

While MICP has shown promise in laboratory settings, particularly with single strains under controlled conditions, its application to the complex matrix of HPW remains largely unexplored [19,20,23]. Continuous-flow operation remains unfeasible, and the application of MICP strategies for hardness removal from produced water is still in its embryonic stage. The harsh salinity, recalcitrant organics, and fluctuating water chemistry characteristic of HPW present formidable barriers that challenge the robustness and scalability of existing MICP strategies [16,24–26]. By shifting from single-strain systems to top-down assembled engineering microbiomes cultivated through iterative environmental stress conditioning [27], the goal is to overcome the core limitations of existing biological treatments for HPW.

At the mechanistic level, recent studies highlight extracellular polymeric substances (EPS) as the principal sites initiating mineral nucleation [28]. EPS is a gel-like matrix composed of polysaccharides, proteins, and other biopolymers secreted by microorganisms, and it plays a pivotal role in this process. EPS and the cell wall together create a scaffold rich in negatively charged functional groups that effectively bind cations such as Ca^{2+}. This localized accumulation of ions renders EPS the primary nucleation site for carbonate mineral formation. However, the interfacial regulatory mechanisms governing specific nucleation sites remain unelucidated. Notably, intracellularly controlled mineralization pathways, as a potential hardness removal strategy, have long remained a research blind spot [29,30]. This process involves mineral deposition within the cytoplasmic or periplasmic regions of microorganisms and often exhibits a controlled amorphous-to-crystalline phase transition. Such intracellularly regulated transformations could have substantial implications for Ca^{2+} and Mg^{2+} removal in HPW [31]. A deeper mechanistic understanding of both extracellular and intracellular pathways is essential for unlocking the full potential of MICP in high-salinity scenarios.

This study aims to: (i) Achieve a technological breakthrough in the continuous precipitation of hardness ions from HPW through construction of an engineering microbiome; (ii) Elucidate the removal patterns of organic functional groups under salinity perturbation; (iii) Identify critical nucleation sites and unravel the underlying microbial biomineralization mechanisms. The findings are expected to contribute to an environmentally sustainable and industrially scalable solution for HPW treatment, advancing the engineering implementation of MICP technology in complex field environments.

2. Materials and methods

2.1. Reagents and materials

The HPW used for testing was sourced from the Xinjiang Uygur autonomous region Chunfeng Oilfield of Sinopec, China. The water samples were transported and stored through a cold chain and kept at −20 °C. The 50 % and 75 % HPW used in both batch and continuous operation tests were prepared with ultrapure water and a predetermined amount of sodium acetate was added to maintain consistent chemical oxygen demand (COD) levels across different dilution ratios of HPW. All reagents used were at least analytical grade and prepared in ultrapure water (HyperpureX, China). See the Supporting Information Text S1 for a complete chemical list and information.

2.2. Analysis methods

The water quality indicators of HPW were tested. Ca^{2+} and Mg^{2+} were determined using atomic absorption spectrophotometry. NH_4^+-N was detected using ultraviolet spectrophotometry. Urea was quantified by the diacetyl monoxime method coupled with UV spectrophotometry. [32] COD in HPW was determined using rapid digestion spectrophotometry and TPHs were determined using gas chromatography (GC, Agilent 8890, USA). [26] Heavy metals and trace elements in HPW were determined using inductively coupled plasma-mass spectrometry (ICP-MS, Agilent 720ES(OES), USA). The water quality parameters were detailed in Table S1. For other analytical methods and parameters, see Text S5.

2.3. Batch experiment and continuous-flow operation test

The mineralization potential and maximum capacity of the microbiome pre-adapted to long-term exposure to produced water were systematically evaluated. The feasibility and maximization of MICP process for HPW softening was investigated using a three-factor, four-level orthogonal experiment combined with activated sludge recycling tests. The key operational factors included initial sludge concentration, urea dosage, and number of sludge recycling cycles, aiming to maximize process efficiency and to elucidate the relationship between operating conditions and mineralization performance. The specific experimental

setup is detailed in Table S2.

Continuous-flow precipitation of Ca^{2+} and Mg^{2+} from heavy-oil produced water was carried out using a sequencing batch reactor (SBR). Inoculum was collected from surface marine sediment at the station of A4 (123°2′848″ E, 36°0′614″ N) of the Yellow Sea. The initial microbiome was regulated and developed using produced water for more than 450 days to ensure tolerance to the extreme saline and organic conditions of the feed water.

The experiment for the removal of Ca^{2+} and Mg^{2+} from HPW was conducted in three phases: the 50 % HPW adaptation phase (0–20 days), the 75 % HPW stabilization phase (21–60 days), and raw HPW operation phase (61–90 days). Additionally, a predetermined dosage of urea (5 g/L, 8 g/L, and 10 g/L) was added at each phase to ensure sufficient carbonate content in the system. The continuous operation of the reactor was divided into two periods: the calcium and magnesium precipitate discharge period (0–36 days) and the fresh sludge replenishment period (37–90 days). Concurrently established sludge replenishment (SR) reactor without urea to periodically replenish activated sludge for the MICP reactor (5 % of the reactor's working volume replenished every 3 operational cycles), with continuously fed with HPW as influent. Added 38 $mg \bullet L^{-1}$ of potassium dihydrogen phosphate to maintain the phosphorus requirements of microorganisms. The initial sludge volume index (SVI_5) was $84.6 \pm 5.2\ mL \bullet g^{-1}$ and the mixed liquid suspended solid (MLSS) content was $10.0 \pm 1.2\ g \bullet L^{-1}$. Both reactors were operated under a 24 h cycle configured with a 23 h aeration phase; a 1 h integrated phase incorporating sludge settling, effluent discharge, and influent replenishment.

Sludge samples were collected from the MICP reactor systems at 8-day intervals (specifically on days 1, 9, 17, 25, 33, 41, 49, 57, 65, 73, 81, and 89) for subsequent 16S rRNA gene sequencing to characterize microbiome. Bacterial genomic DNA was extracted from sludge samples using PowerSoil DNA isolation kit. Urease activity levels in sludge samples were measured using a urease activity assay kit (Solarbio, China). Loosely-bound EPS (LB-EPS) and tightly-bound EPS (TB-EPS) were sequentially extracted from the mixed liquor sample collected on Day 73 using the heating method [33]. After centrifugation at 4000 rpm for 5 min, the supernatant was removed to obtain the sludge sediment. The sediment was diluted to its initial volume with 0.05 % NaCl preheated to 50 °C, shaken for 1 min, and centrifuged again at 4000 rpm for 5 min; the filtrate of the supernatant through a 0.7 μm glass-fiber membrane was collected as LB-EPS. The remaining sediment was then rediluted with 0.05 % NaCl, heated at 60 °C for 30 min in a water bath, and centrifuged at 4000 rpm for 5 min. The resulting supernatant, after filtration with the same membrane, was obtained as TB-EPS.

2.4. Organic-inorganic composite characterizations

The crystal structure of dried sludge (DS) was analyzed using X-ray diffraction (XRD; Rigaku SmartLab SE, Japan). Vibrational signatures of calcium-magnesium carbonates in DS were characterized using Raman spectrometer (Raman, Horiba LabRAM HR Evolution, Japan) and FTIR (FTIR, Nicolet iS50) to identify mineralogical phase transitions. For organic component analysis, 50 mL of liquid sample was collected from a representative operational cycle and filtered through a 0.22 μm nylon membrane to remove suspended solids. The filtrate was subsequently freeze-dried (SCIENTZ-10N, China) and redissolved in 1 mL of deionized water to concentrate the organic constituents. A small aliquot of this concentrated solution was directly deposited onto an attenuated total reflectance (ATR) crystal surface for spectral examination of the organic functional groups present in HPW. Representative samples of suspended activated sludge and sedimentary aggregates from the aeration phase were sequentially collected during reactor operation. Ultrathin sections (70–90 nm) were prepared through a standardized protocol involving fixation, dehydration, resin embedding, and ultramicrotomy, following established ultramicrotomy protocols. The mineral morphology was observed using high-resolution transmission electron microscopy (HRTEM) and analyzed using selected area electron diffraction (SAED). After dual staining with uranyl acetate and lead citrate, microbial-mineral interactions were visualized using high-angle annular dark-field scanning transmission electron microscopy (HAADF-STEM) (S/TEM, Talos F200X, Thermo Fisher Scientific, USA) to elucidate the microstructural and elemental features involved in MICP process. The specific operation method could be found in Text S4.

2.5. Theoretical calculation method

The molecular dynamics simulations were conducted in Materials Studio 2020. A computational model encompassing Ca^{2+} ions, H_2O molecules, and carbonate ion (CO_3^{2-}) anions was initially constructed, with atomic charges assigned via the charge equilibration method and geometrically optimized using the Forcite module under stringent convergence criteria (energy change $< 1 \times 10^{-3}$ kcal/mol; force tolerance < 0.05 kcal/(mol·Å)). The amorphous configuration was subsequently generated using the Amorphous Cell module, employing periodic boundary conditions and an initial density of 1.023, 1.500, 2.000, 2.590 g/cm^3 to align with ACC structural data. Simulations were performed under the NVT ensemble regulated by a Nose-Hoover thermostat at 298 K, utilizing the COMPASS II force field to describe interatomic interactions. A time step of 1 fs and a total simulation duration of 50 ps ensured temporal resolution of dynamic processes, while long-range electrostatic interactions were treated via the Ewald summation method with a 12.5 Å cutoff for van der Waals forces. Determined the hydrogen bond length of the system through the radial distribution function (RDF) of critical atom pairs (O_{Water}—H, $O_{Carbonate}$—H) and analyzed the changes in bond length and bond angle of hydrogen bonds during dehydration process.

3. Results and discussions

3.1. Batch experimental study on hardness removal of HPW

To determine the potential and maximum capacity of the microbiome to precipitate Ca^{2+} and Mg^{2+} from HPW through MICP process, response surface methodology was employed for parameter optimization (denoted as X: urea dosage, Y: initial MLSS concentration, and Z: HPW dilution ratio). The Box-Behnken design and corresponding response surface profiles depicting Ca^{2+}/Mg^{2+} precipitation efficiencies in batch experiments are presented in Fig. 1a and b, respectively. A robust quadratic regression model was established to characterize the relationship between dependent variables and independent factors, expressed through the following second-order polynomial equation:

$$\begin{aligned} Ca^{2+}\ \text{precipitation}\ (\%) = & -6.438 + 17.638X \\ & + 5.867Y - 2.703Z - 0.063XY - 0.046XZ \\ & + 1.023YZ - 1.207X^2 - 0.394Y^2 - 0.566Z^2 \end{aligned}$$

$$\begin{aligned} Mg^{2+}\ \text{precipitation}\ (\%) = & -51.832 + 20.866X + 9.866Y + 42.379 \\ & Z + 0.047XY - 0.867XZ - 1.323YZ - 1.477X^2 - 0.462Y^2 - 13.074Z^2 \end{aligned}$$

The established mathematical model revealed characteristic peak-shaped response surfaces, demonstrating significant interactive effects among the operational parameters. Eccentricity analysis of elliptical contours highlighted the critical influence of initial urea concentration on precipitation kinetics. Among all factors, the MLSS exerted dominant control over Ca^{2+} removal, whereas its effect on Mg^{2+} precipitation was relatively limited. This discrepancy originates from the intrinsic hydration properties of the two cations. Mg^{2+} possesses a stronger affinity for water molecules and forms a more stable hydration shell that is difficult to disrupt [34]. Consequently, even with elevated MLSS levels, Mg^{2+} remains less prone to dehydration and reaction with CO_3^{2-} to form stable precipitates. In contrast, Ca^{2+}, with its lower dehydration energy,

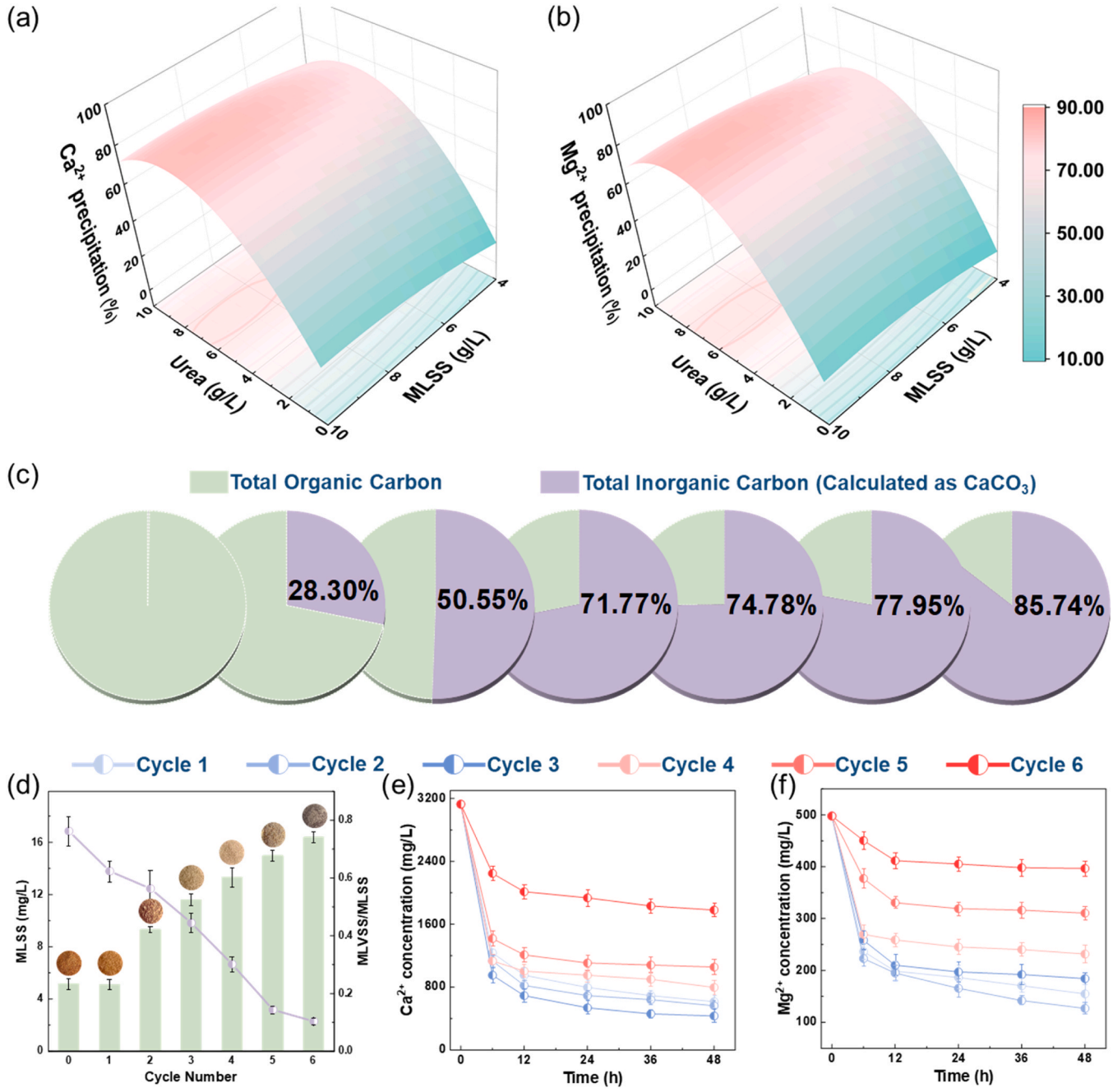

Fig. 1. The MICP potential and maximum capacity of microbiome: (a) Response surface analysis of Ca^{2+} and (b) Mg^{2+} precipitation after 216 h treatment time; Recycling limits and continuous operation parameter optimization of microbiome: (c) The morphology and changes in inorganic carbon (calculated as $CaCO_3$) and organic carbon composition of dried sludge from six cyclic experiments, (d) MLSS and MLVSS/MLSS (illustrated as dried sludge morphology), (e) Ca^{2+}, (f) Mg^{2+} precipitation efficiency.

can more readily release coordinated water molecules, thereby facilitating carbonate precipitation. Although previous studies have emphasized the decisive role of pH in hardness-ion precipitation efficiency—and ureolysis theoretically elevates system pH through ammonia generation [31]. This study found that initial urea concentrations (0 −10 g/L) caused only minor pH fluctuations in HPW – increasing from 7.45 ± 0.04–8.59 ± 0.05 (Fig. S1). This increase was markedly lower than that of conventional MICP systems, indicating the buffering capacity of the microbiome played a dominant role in pH regulation. Such self-buffering behavior enabled efficient co-precipitation of Ca^{2+} and Mg^{2+} under neutral to weakly alkaline conditions, avoiding the extreme pH shifts common in pure culture systems.

A six-cycle preliminary experiment was conducted under optimized conditions to evaluate microbiome adaptability and process stability under elevated hardness-ion loads. Throughout six consecutive operational cycles, the DS exhibited marked phase-dependent transformations in both morphological structure and compositional profiles (Fig. 1c): (i) DS exhibited color transitions, evolving from bright yellow (Cycles 0–3: organic dominance) through grayish-white (Cycles 4–5: organic-inorganic composites) to dark gray (Cycle 6: mature Ca-Mg mineral composites); (ii) TIC content surged from 0.03 % to 10.28 % (w/w), with total inorganic carbon calculated as calcium carbonate escalating from 0.29 % to 85.74 %, indicating near-complete biomass calcification.

The MLVSS/MLSS underwent rapid depletion (0.76–0.10), confirming inorganic component dominance and functional incapacitation of calcified biomass (Fig. 1d). During the initial three operational cycles (Fig. 1e and f), Ca^{2+} precipitation efficiency progressively increased, reaching 86.17 %. As the removal rate plateaued (<5 % increase between 24–48 h), the optimal reactor cycle was set to 24 h. However, systemic performance deterioration emerged during cycles 4–6, with Ca^{2+} removal declining to 43.08 %. Similarly, Mg^{2+} precipitation efficiency collapsed earlier. The critical determinant for sustaining the long-term stability of MICP system resides in: (i) construction and acclimatization of HPW-adapted engineering microbiome through phased substrate exposure, and (ii) implementation of bioaugmentation strategy to counteract biomass attrition, with optimization trails recommending precipitate discharge at every 3 operational cycles to mitigate process inhibition caused by carbonate accumulation.

XRD analysis revealed the progressive evolution of the crystalline structure of DS during the MICP process (Fig. 2a). The initial sludge exhibited a prominent amorphous organic feature near $2\theta = 20°$, while its inorganic phase consisted exclusively of a single calcite phase (PDF#86–2334) with high crystallinity. After 6 h of mineralization, diffraction peaks corresponding to monohydrate calcite (PDF #83–1922) and aragonite (PDF #41–1475) intensified, accompanied by the emergence of amorphous calcium carbonate as a transient precursor. With prolonged mineralization, the XRD pattern revealed a more complex mineral assemblage, including the emergence of Mg-enriched calcite (PDF#86–2335). A characteristic peak shift ($\Delta 2\theta = +0.15°$) was identified for the calcite (104) plane, corresponding to a reduction in interplanar spacing from 0.304 nm to 0.302 nm. This phenomenon was mechanistically attributed to lattice substitution, where smaller Mg^{2+} (0.72 Å) partially replace Ca^{2+} (1.00 Å) at approximately 6.6 % substitution ratio [35]. These findings provided structural evidence for Mg^{2+} displacement pathways in HPW system. The lattice vibrational characteristics of biogenic carbonate minerals were elucidated through laser Raman spectroscopy (Fig. 2c). The spectra revealed three dominant vibrational modes of calcium carbonate crystals: a prominent ν_1 symmetric stretching vibration at 1086 cm^{-1}, a ν_4 bending vibration at 279 cm^{-1}, and a broadened ν_3 antisymmetric stretching vibration centered at 1386 cm^{-1} [36,37]. Notably, a diffuse peak observed in the high-frequency region (1505 cm^{-1}) was assigned to the ν_3 vibrational mode of CO_3^{2-} groups in magnesium carbonate. However, the spectra exhibited significant metastable crystallization features accompanied by enhanced background noise, attributable to organic matrix modulation during biomineralization process [38]. The FTIR spectral evolution of sludge exhibited analogous characteristics (Fig. 2d). The initial DS displayed rich organic functional group distributions, including hydroxyl, carboxyl, and amino groups. With prolonged contact time, characteristic absorption peaks of organic functional groups showed significant attenuation or disappearance, while carbonate mineral phase signatures became prominent in the CO_3^{2-} vibrational region [36]. This synergistic evolution of organic component decay and inorganic mineral formation revealed the oriented crystallization mechanism of carbonate minerals at bio-organic interfaces mediated by microbial metabolic activity.

The organic–inorganic composite structure of the mineralized products generally exhibited irradiation damage under electron beam exposure (intact regions shown in Fig. 2b). The carbonate products exhibited aggregated micro-architectures composed of densely packed nanocrystals with poorly defined boundaries and fibrous or reticular morphologies. These features likely arise from the spatial confinement imposed by organic templates during bacterial mineralization, promoting oriented crystal growth. SAED patterns revealed distinct polycrystalline diffraction rings. Through crystallographic plane indexing, diffraction signals corresponding to *hkl*= 0,0,3 (d=5.67 Å), 0,1,2 (d=3.85 Å), and 0,0,6 (d=2.84 Å) for #2 were identified as being in precise agreement with standard calcite lattice spacings. Combined with morphological characteristics, these findings confirm the predominant existence of nanoscale crystalline structures within the samples that exhibit short-range order but long-range disorder.

3.2. Continuous operational performance of MICP process for HPW treatment

This study achieved the first industrial continuous removal of Ca^{2+} and Mg^{2+} in HPW through MICP process, constructing an operational system for synchronous calcium-magnesium co-precipitation. As illustrated in Fig. 3a, a period optimization strategy was implemented involving dynamic separation of calcified sludge during the precipitate

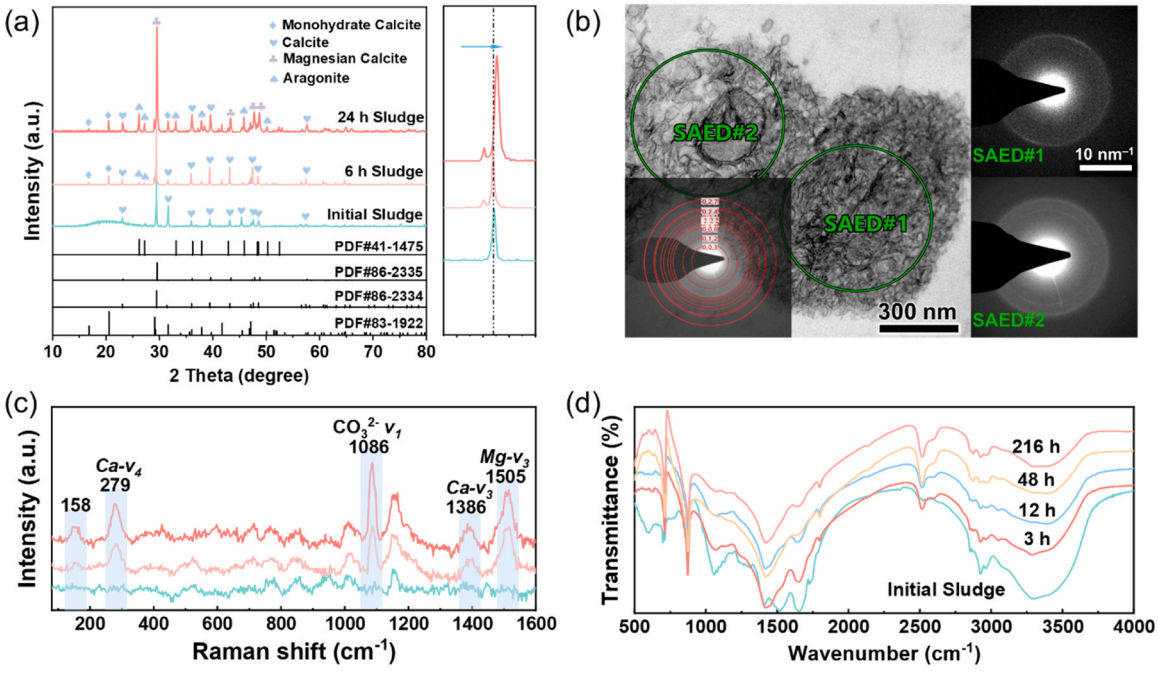

Fig. 2. Mineral phase transformation at organic-inorganic interfaces: (a) XRD; (c) Raman and (d) FTIR spectra of dried sludge at different contact times; (b) High resolution TEM and SAED analysis of mineralized products.

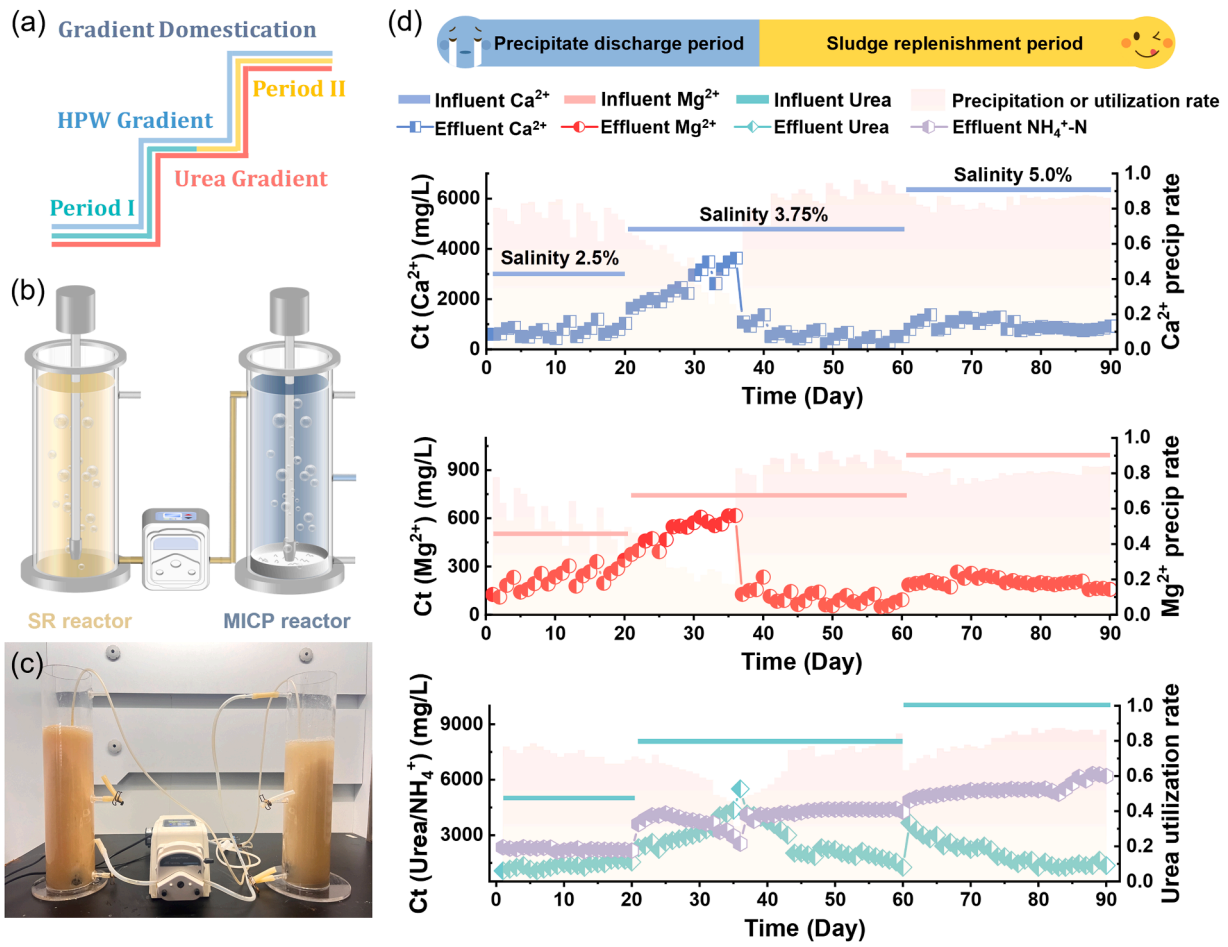

Fig. 3. Construction of engineering microbiome: (a) Gradient optimization strategy for HPW softening continuous-flow operation; (b) Reactor configuration including a sludge replenishment reactor and a microbial induced calcium carbonate precipitation reactor; (c) Photograph of the actual reactor setup; (d) Continuous operational performance: Ca^{2+}/Mg^{2+} precipitation efficiency, urea residual concentration and ammonia nitrogen release levels.

discharge phase, combined with an active sludge-replenishment mechanism. The system synergistically regulated HPW concentration gradients and urea dosage. The SR reactor delivered fresh active sludge via a peristaltic pump, effectively maintaining microbiome activity (Fig. 3b and c).

Operational data demonstrated distinct performance periods (Fig. 3d). During the initial precipitate discharge stage (Days 0–20), calcium and magnesium removal efficiencies reached 82.3 % and 78.5 %, respectively, under 50 % HPW loading. However, increasing the load to 75 % caused significant system destabilization due to insufficient carbonate buffering capacity, reducing magnesium precipitation efficiency to below 20 %. Implementing a cyclic sludge renewal strategy (Days 37–90) restored divalent cation precipitation functionality within 48 h, maintaining precipitation rates above 80 % during continuous operation. Besides, the system maintained stable long-term efficiencies of 87.28 % for Ca^{2+} and 84.16 % for Mg^{2+} under full-load conditions (100 % raw HPW). NH_4^+-N concentration derived from ureolysis exhibited a significant positive correlation with calcium-magnesium precipitation efficiency. Nevertheless, excessive NH_4^+-N accumulation (>6000 mg/L) induced dual challenges of nitrogen loss and secondary contamination risks. An electro-enhanced Donnan dialysis process was employed to recover ammonium, a byproduct of the MICP process, in the form of ammonium sulfate, and to further precipitate the residual Ca^{2+} and Mg^{2+} as sulfates (Fig. S6 and S7). This integration achieved efficient nitrogen recovery and minimized secondary pollution, further improving process sustainability.

Beyond hardness-ion removal, the MICP reactor demonstrated a robust capacity for simultaneous degradation of refractory hydrocarbons. During a typical operational cycle, TPHs concentration decreased significantly from 65.74 mg L^{-1} to 6.92 mg L^{-1}, corresponding to an 89.5 % removal efficiency. Continuous operation maintained this high level of performance. GC analysis revealed microbial degradation exhibited carbon chain-length selectivity (Fig. S9), with residual components predominantly comprising long-chain hydrocarbons (>C36), while degradation efficiencies exceeded 95 % for medium and short-chain alkanes (<C20).

To investigate the organic degradation pathways in produced water under calcium-magnesium perturbation, *in situ* ATR-FTIR was employed for dynamic monitoring of HPW, coupled with two-dimensional correlation spectroscopy (2DCOS) to elucidate component evolution. Spectral analysis of raw HPW revealed characteristic peaks corresponding to −CH (2920 cm^{-1}, 2850 cm^{-1}), C═C (1375 cm^{-1}, 1455 cm^{-1}), and −CHO (870 cm^{-1}) functional groups, confirming that its organic components were mainly composed of alkanes and alkenes with minor aldehydes (Fig. 4a). Upon prolonged microbial-substrate interaction, these characteristic peaks exhibited progressive attenuation and completely disappeared within 24 h [39]. While new absorption features corresponding to the C–O vibration doublets (1045 cm^{-1}, 1085 cm^{-1}) and a broad −COOH peak (995 cm^{-1}) emerged sequentially before diminishing during further mineralization. This spectral evolution demonstrates that the organic matter in HPW underwent a transformation from hydrophobic hydrocarbons to hydrophilic oxygenated compounds, clearly revealing a stepwise oxidative degradation pathway of "alkanes → alcohols → carboxylic acids." Among these intermediates,

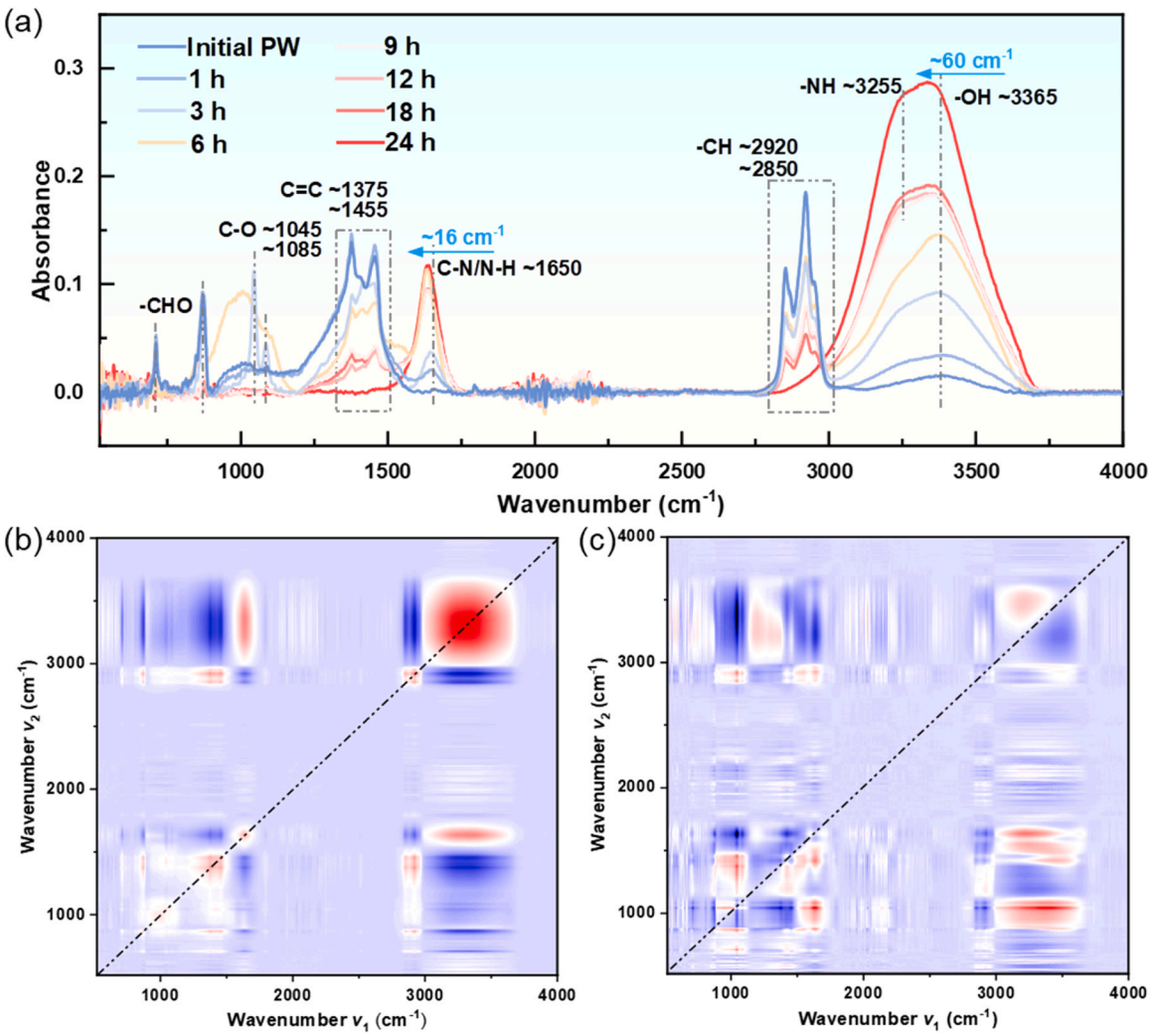

Fig. 4. (a) *In situ* ATR-FTIR during a typical HPW treatment cycle, (b) synchronous two-dimensional correlation spectroscopy, and (c) asynchronous two-dimensional correlation spectroscopy.

alcohols and carboxylic acids are transient species with short residence times, yet their appearance is essential for elucidating the degradation mechanism. During the reaction, the −OH stretching band (3365 cm^{-1}) intensified and shifted by approximately 60 cm^{-1} toward higher frequency. This blue shift reflects reorganization of the hydrogen-bond network induced by charge-guided coordination between Ca^{2+}/Mg^{2+} and water molecules. Concurrently, the formation of amorphous $CaCO_3$ generated structured hydration layers with high water-binding capacity [40]. The synergistic interaction between these mechanisms induced dipole moment alteration and vibrational mode restructuring of O−H bonds. Concurrently, sustained intensification of −NH stretching vibrations (3255 cm^{-1}) and C−N/N − H bending vibrations (1650 cm^{-1}) was observed, which exhibited high consistency with the characteristic spectral profiles of EPS produced during microbial metabolism. The interactions between functional groups and the temporal sequence of reactions in dynamic systems are elucidated by employing synchronous and asynchronous 2D-COS (Fig. 4b and c). The sequential order of functional group responses was as follows: carbonyl groups → ether linkages → amino groups → carboxylic acids → hydroxyl groups → aldehyde groups → alkyl groups → imine groups [41]. This sequence aligns precisely with a cascade mechanism involving bond cleavage, oxidation of intermediates, and subsequent microbial metabolic activation, illustrating the synergistic coupling between organic degradation and biomineralization in the MICP system.

3.3. EPS induced extracellular biomineralization

In microbially mediated biomineralization, the preferential nucleation of mineral crystals is tightly associated with EPS and surface-bound functional proteins secreted by microorganisms. EPS, enriched with anionic functional groups such as carboxyl, hydroxyl, and phosphoryl moieties, serves as a dynamic scaffold that regulates the physicochemical microenvironment for nucleation. A crucial step in the mineralization process is the disintegration or partial reorganization of EPS, which locally disrupts the metal-binding equilibrium. This leads to a surge in free cation concentration, surpassing the solubility product and triggering localized supersaturation—a prerequisite for nucleation. The release of these cations in confined microenvironments ensures spatially controlled, oriented deposition of minerals, often following the templating patterns of the microbial EPS network [28,30]. The FTIR of EPS was investigated to examine differences and evolution during continuous-flow operation (Fig. 5a). During the precipitate discharge period, the abundance of organic functional groups (e.g., C−O, C−N) in LB-EPS exhibited a significant decline with prolonged contact time, while the characteristic peaks of Ca^{2+}−COO^{-} complexes continuously intensified, indicating that specific binding between calcium ions and carboxyl groups predominated the component reorganization of LB-EPS during this phase [42]. Upon entering the sludge replenishment period, the abundance of $-COO^{-}$ groups, polysaccharide-, and protein-associated functional groups in LB-EPS exhibited a marked

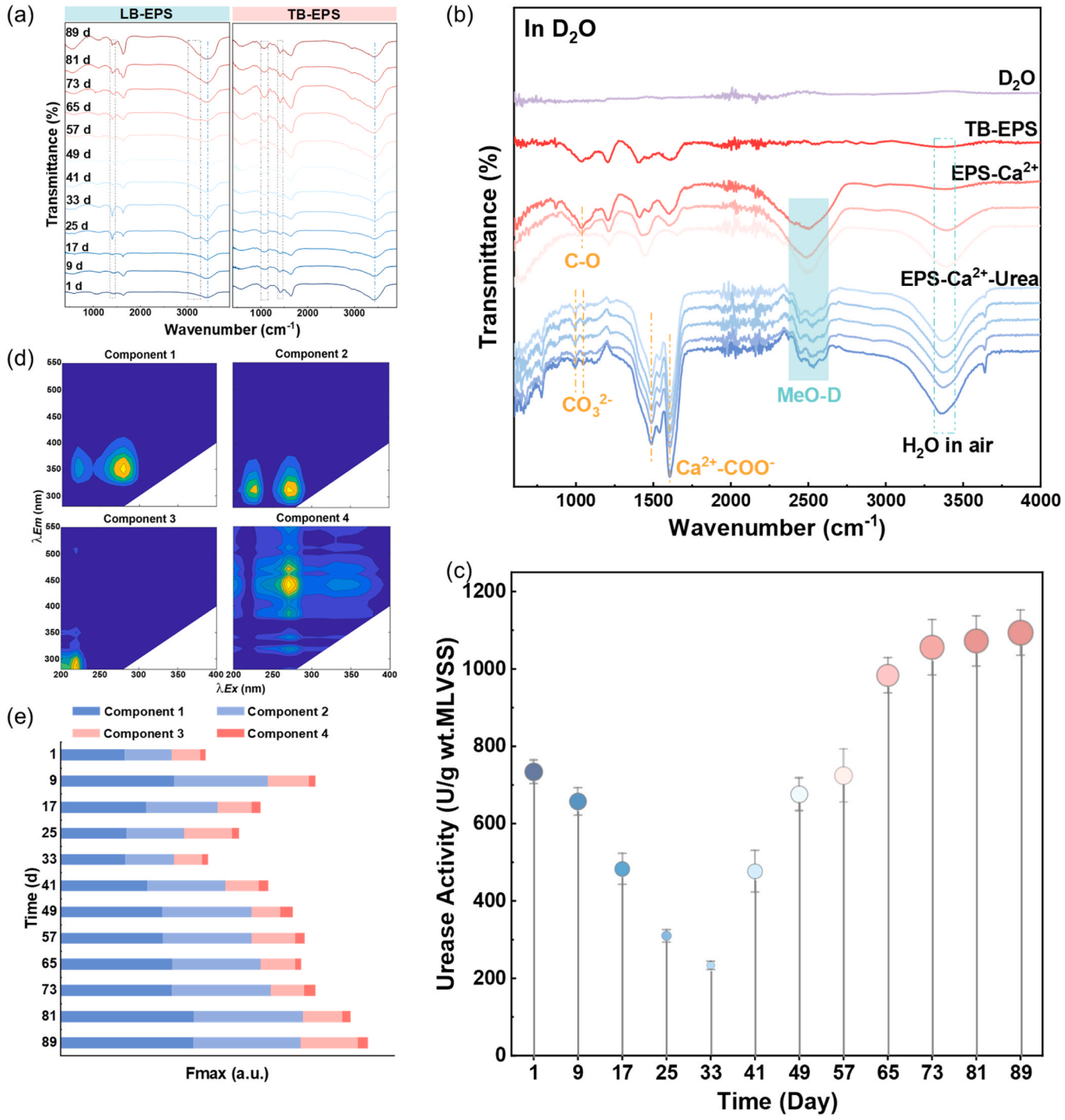

Fig. 5. (a) FTIR spectra of LB-EPS and TB-EPS at preset sampling time points; (b) In situ ATR-FTIR analysis of functional group contributions in TB-EPS under a D_2O background to calcium carbonate precipitation (measurement time points: 10 s, 30 s, 1 min after Ca^{2+} addition; 10 s, 30 s, 1 min, 5 min, 10 min after urea addition); (c) Microbial urease activity at preset sampling time points; (d) Fluorescent species composition and (e) intensity variations of TB-EPS analyzed by 3D-EEM combined with PARAFAC.

recovery, revealing periodic regeneration behavior in its compositional profile. In contrast, the infrared characteristic peaks of TB-EPS showed no significant attenuation during continuous operation and its functional group stability was notably superior to that of LB-EPS, which was closely associated with its tightly matrix-encapsulated structure and high-efficiency regeneration capability driven by microbial metabolic activity [33]. The 3D-EEM fluorescence analysis of EPS further corroborated these findings (Fig. S10). These distinctions demonstrated that LB-EPS, due to its spatial distribution and weaker binding strength, was more susceptible to inactivation under liquid-phase environmental perturbations, whereas TB-EPS maintained long-term protective functions for sludge flocs through its stable structural configuration.

In situ ATR-FTIR spectroscopy provided detailed molecular insights into the role of TB-EPS during MICP process, especially under isotopic substitution conditions (Fig. 5b). Given the spectral overlap between surface hydroxyl stretching vibrations and bulk water signals, deuterium oxide (D_2O) was employed as the solvent to suppress the interference from hydrogen-bonded H_2O. In D_2O, −OH groups were isotopically

replaced by −OD, manifesting characteristic bands at 2460 and 1200 cm^{-1} (Fig. S11), which exposed previously hidden surface interactions. Under neutral pH (without urea), surface hydroxyl groups of TB-EPS preferentially coordinated with Ca^{2+} to form stable metal–hydroxyl–deuterium (MeO–D) complexes [43], initiating local Ca^{2+} enrichment. Upon urea hydrolysis, these complexes acted as transient reservoirs, gradually releasing cations that were subsequently redirected towards deprotonated carboxylate groups ($-COO^-$). The enhanced asymmetric stretching vibrations at 1485 and 1605 cm^{-1} confirm this activation and binding, signifying a sequential cation transfer from hydroxyl to carboxyl groups. This two-stage mechanism enhanced local Ca^{2+} concentration and spatial precision of heterogeneous nucleation. The strong ion-dipole interactions between Ca^{2+} and $-COO^-$ groups provided a thermodynamically favorable interface for the nucleation of calcium carbonate polymorphs [44]. As a result, the crystal phase distribution of aragonite and calcite within EPS matrix was regulated by the chemical heterogeneity and spatial arrangement of functional groups, underscoring the dual role of EPS as both ion reservoir and structural template.

Through 3D-EEM fluorescence spectroscopy combined with PARAFAC, we deciphered the composition and intensity variations of fluorescent components during continuous operation (Fig. 5d and e). Component 1 exhibited fluorescence maxima at excitation/emission (Ex/Em) wavelength pairs of 275/350 nm and 225/350 nm, characteristic of tryptophan and tyrosine residues, respectively [45]. Component 2 displayed an approximately 20 nm blue shift in emission wavelength relative to Component 1. This spectral transition originated not from novel fluorophores, but arose through coordination complexation between amino acids in Component 1 and Ca^{2+} or Mg^{2+}, where molecular conformational reorganization induced characteristic fluorescence peak displacement. The formation of these metal-organic complexes potentially facilitates oriented carbonate nucleation via interfacial charge modulation. During the initial adaptation phase, synchronized increases in both free and metal-complexed amino-acid signals indicated rapid microbiome acclimation. The subsequent precipitate discharge period showed gradual attenuation of both components due to metabolic-physiological disequilibrium between amino acid replenishment and biomineral export rates. After sludge replenishment, with the recovery of EPS synthesis metabolism in the MICP reactor, its intensity rebounded to a significant level. The concurrent improvement in Ca^{2+} and Mg^{2+} precipitation confirmed that amino-acid dynamics within EPS actively regulate mineralization processes. Component 3 (Ex/Em 220/275 nm) served as a spectroscopic characteristic of aromatic compounds in HPW influent. Component 4 (Ex/Em 275/450 nm) was identified as humic-like substances, indicative of refractory organics accumulation from either microbial byproducts or HPW [24].

As the pivotal enzyme catalyzing the hydrolysis of urea, urease plays a central role in modulating the local alkalinity and CO_3^{2-} concentrations essential for MICP reactions in HPW [46,47]. Monitoring data indicated a marked decline in urease activity from 733.95 U/g MLVSS at the initial operational stage to a minimum of 233.32 U/g by day 33, reflecting a significant attenuation of the microbiome's mineralization capacity under sustained stress. This reduction was attributed primarily to the encrustation effect, wherein carbonate deposits accumulated on cell surfaces and within biofilms, impeding substrate diffusion and metabolic exchange. However, implementation of a sludge replenishment strategy effectively restored enzymatic activity, resulting in a dramatic rebound of urease activity to 1093.66 U/g MLVSS by the end of the operational period. This represents a 368.74 % increase from the minimum level and even exceeds the initial enzymatic activity (Fig. 5c). This recovery confirmed that biomass renewal mitigated mineral encrustation and restored enzymatic functionality. The findings underscore that excessive carbonate encrustation severely constrains microbial metabolism, whereas controlled biomass replacement sustains urease activity and overall system alkalinity. Furthermore, this strategy provides practical insights for scaling up MICP in continuous-flow systems. By incorporating adaptive operational controls such as periodic biomass refreshment, microbial activity and system alkalinity can be consistently sustained, ensuring reliable long-term performance under fluctuating chemical loads. This highlights the critical need to balance biomineralization intensity and microbial viability, particularly in engineered bioreactors treating chemically extreme wastewaters like HPW.

3.4. Microbial controlled intracellular biomineralization

Microbially controlled intracellular biomineralization occurs within specialized subcellular compartments, where bacteria precisely regulate the synthesis of crystalline or amorphous mineral phases through metabolic microdomains that dictate nucleation geometry, textural anisotropy, and spatial orientation [30].

At low magnification (Fig. 6a), the topological distribution of bacterial cells and associated EPS was visualized, while progressive magnification (Fig. 6b–c) revealed a well-defined interface between the microbial cell wall and extracellular polymeric substances, underscoring the spatial complexity of biomineralization microenvironments. Elemental mapping (Fig. 6e) revealed that Ca and Mg elements were broadly distributed along the organic matrix, suggesting that EPS provides an extensive ionic binding scaffold. Interestingly, Mg signals exhibited a markedly higher accumulation within intracellular compartments than the more diffusely distributed Ca, suggesting the presence of selective intracellular sequestration mechanisms. As an essential cofactor for numerous enzymes [48], Mg^{2+} is actively transported into cells through magnesium pumps (mgTE (Table S7)), where it reversibly binds to metabolic components and thus accumulates intracellularly. In contrast, Ca^{2+} primarily interacts with the cell membrane and remains largely confined to the extracellular space. This selective enrichment underscores compartmentalized metabolic pathways that regulate the formation of intracellular mineral precursors [49]. High-resolution STEM imaging of the EPS-rich regions failed to reveal lattice fringes, a limitation attributed to the beam sensitivity of biological samples and dynamic vibration under irradiation. Corresponding SAED patterns (Fig. 6 h) showed diffuse diffraction rings, suggesting the presence of non-crystalline phases. These results, together with the low atomic contrast observed in elemental mapping, provided strong evidence for the presence of ACC and AMC [50].

Significantly, Fig. 6e–f demonstrated pronounced intracellular enrichment of nitrogen and phosphorus, confirmed by elevated Kα signal intensities. The intracellular compartment not only serves as a metabolic center, but also as a transient storage site for mineral precursors. The presence of intracellularly enriched Ca^{2+} and Mg^{2+} in amorphous states indicates the initiation of a controlled biomineralization pathway within the cell. These intracellular mineral phases likely exist as metastable ACC or AMC, stabilized by intracellular macromolecules or organelle-like vesicles. Such amorphous precursors are thought to be stored temporarily in periplasmic or cytoplasmic compartments where they are shielded from premature crystallization through spatial isolation and chelation. Furthermore, the stabilization of ACC/AMC in intracellular compartments implies a biological strategy to delay nucleation and modulate crystal morphology, thereby offering evolutionary advantages in adaptability and functional mineral assembly. Subsequent vesicular transport and exocytosis may facilitate the relocation of these precursors into extracellular spaces, where environmental triggers such as pH increase promote their transformation into crystalline polymorphs. This intracellular-to-extracellular translocation pathway suggests that microbial cells not only modulate mineral phase through surface-bound EPS interactions but also via a tightly regulated intracellular mineral handling system. Such a dual-regulation mechanism underpins the spatial and phase-specific control of MICP [51].

Taken together, these findings emphasize that extracellular regions act as primary nucleation platforms, whereas intracellular mineral processing serves as the critical upstream regulatory module. The

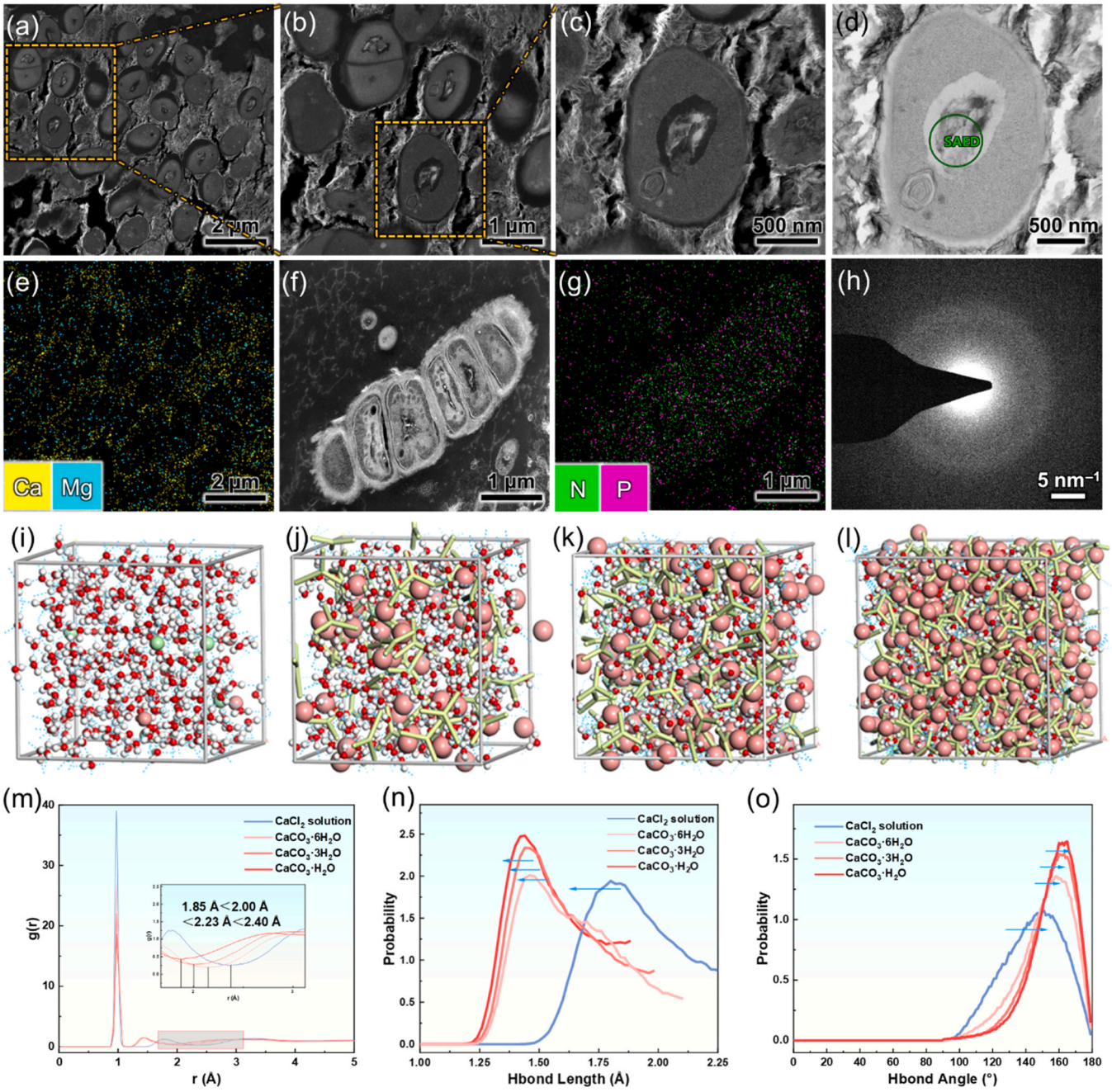

Fig. 6. Suspended microbial samples from the MICP reactor on Day 80 of continuous operation were analyzed for microstructural features. Observations were performed under HAADF-STEM: (a, b, c) Progressively magnified images of bacterial aggregates; (d) Bright-field imaging and SAED acquisition positions; (h) SAED analysis; (f) Bacterial images from alternative locations; (e, g) Elemental mapping of a and f. Molecular dynamics simulation of the enrichment process of Ca^{2+} and CO_3^{2-}: (i) Amorphous model of 5 % $CaCl_2$ solution; (j) $CaCO_3{\cdot}6H_2O$; (k) $CaCO_3{\cdot}3H_2O$; (l) $CaCO_3{\cdot}H_2O$; (m) Radial distribution function analysis of critical atomic pairs; (n) Hydrogen-bond length and (o) Hydrogen-bond angle distribution probability.

establishment of transmembrane ionic gradients and vesicular mineral trafficking allows microorganisms to exert precise spatiotemporal control over polymorph selection and crystal maturation, ultimately influencing the structure and crystallinity of biogenic carbonates.

The evolution of intermolecular hydrogen bonds provides a critical structural probe for understanding MICP process at the molecular scale. Molecular dynamics simulations were employed to elucidate the synergistic reorganization mechanism of the hydrogen-bond network during dehydration. Four amorphous systems were constructed, including a 5 % $CaCl_2$ solution, $CaCO_3{\cdot}6\ H_2O$, $CaCO_3{\cdot}3\ H_2O$, and $CaCO_3{\cdot}H_2O$, initially containing 300 water molecules [52]. As Ca^{2+} concentration gradients established and CO_3^{2-} accumulated through urea hydrolysis, molecular dynamics revealed a marked transition from disordered to ordered configurations. RDF analysis demonstrated stepwise reductions in hydrogen-bond donor-acceptor cutoff distances across dehydration stages (2.40 Å > 2.23 Å > 2.00 Å > 1.85 Å), accompanied by hydrogen-bond contraction from 1.87 Å to 1.43 Å and angular expansion from 151° to 163° (Fig. 6m–o). These coordinated parameter shifts indicated that geometrically constrained $O_{Water}{-}O_{Carbonate}$ hydrogen bonds underwent directional alignment, inducing enhanced rigidity of local coordination environments. Such structural rigidification drove topological rearrangement and densification of the ACC framework. Kinetic trajectory analysis further suggested that this cooperative hydrogen-bond network reconstruction likely reduced nucleation

energy barriers, thereby serving as a structural precursor for amorphous-to-crystalline phase transitions.

3.5. Engineering microbiome analysis

Engineering microbiome succession and compositional during the transition from the precipitate discharge period (Period I) to the sludge replenishment period (Period II) were investigated through 16S rRNA gene sequencing. Venn analysis revealed a 10.7 % increase in total OTUs (Operational Taxonomic Units) from 495 in Period I to 548 in Period II, with the 53 newly acquired OTUs potentially compensating for the loss of keystone functional taxa caused by calcified sludge discharge through functional redundancy mechanisms (Fig. 7a). Further analysis of pCoA results revealed significant separation between the two-phase communities, with Period II samples exhibiting higher aggregation, indicating that sludge supplementation reshaped the stable community structure (Fig. 7b). Neutral community model analysis demonstrated that the R^2 value increased from 0.514 to 0.698 in Period II, accompanied by a 43.6 % elevation in Nm value, suggesting that sludge supplementation shifted community assembly towards stochastic process dominance through enhanced microbial dispersal (Fig. 7d). This elevated stochasticity corresponded with the recovery of Ca^{2+} and Mg^{2+} precipitation, implying that the dispersal, colonization, and recruitment of source functional bacteria constitute the key mechanism maintaining continuous stable operation of HPW hardness removal system. At the phylum level of the microbiome, *Pseudomonadota* consistently maintained a dominant position, with its relative abundance significantly increasing from 34.92 % to 61.92 % during prolonged system operation (Fig. 7c). Members of this phylum are widely recognized as urease-positive bacteria with multifunctional capabilities, including efficient organics degradation, heavy metal biosorption, and microbially induced carbonate precipitation [45]. A microbial co-occurrence network was

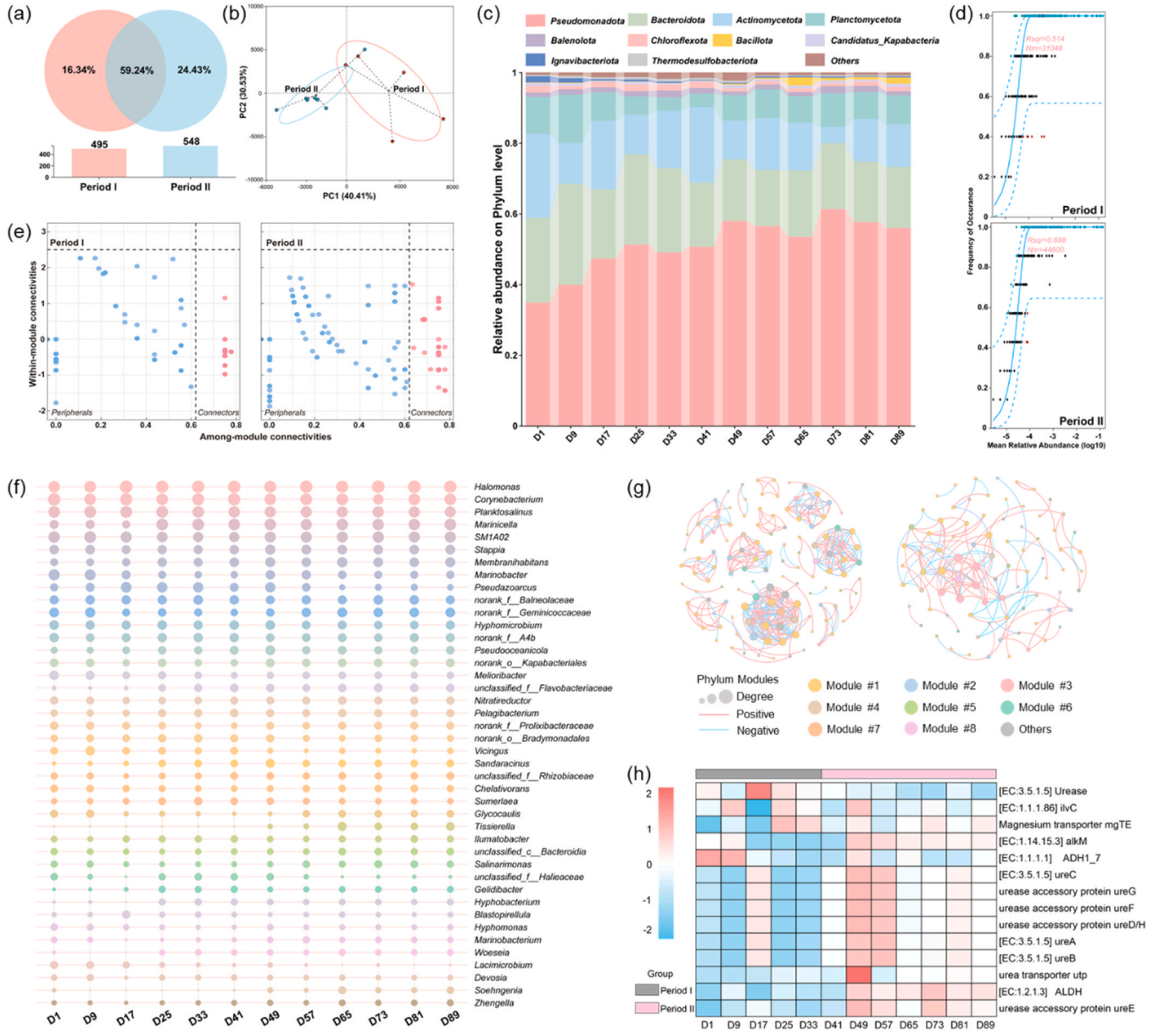

Fig. 7. Engineering microbiome diversity and composition in Period I and Period II: (a) Venn diagram of OTUs overlap; (b) Principal Coordinate Analysis (PCoA) ordination; (c) Taxonomic composition at the phylum level; (d) Neutral community model analysis; (e) Zi-Pi topological role classification of microbial taxa; (f) Taxonomic composition at the genus level; (g) Phylum-level co-occurrence network; (h) KEGG-EC (Kyoto Encyclopedia of Genes and Genomes-Enzyme Commission) functional annotation of MICP-associated enzymatic gene clusters.

constructed at the phylum level to visualize the internal relationships of the microbiome (Fig. 7 g). In Period II, the node decreased from 121 to 83, indicating a microbiome transition from highly complex diversity to a structure dominated by critical functional taxa. The number of connected components decreased from 29 to 15, reflecting enhanced network connectivity and intensified functional modular cooperation within the community, which reduced inefficient metabolic activities of isolated subpopulations. The proportion of positive correlation edges increased from 63.69 % to 68.0 %, demonstrating a more mutualistic interactions among microorganisms. For instance, *Pseudomonadota* and *Bacillota* exhibited synergistic resistance to extreme environments and participated in MICP. Furthermore, modularity decreased from 0.826 to 0.709, suggesting a structural transformation from highly modular clusters to cross-module collaboration. This reorganization reduced resource competition or inhibitory interactions, minimized metabolic redundancy, and prioritized energy allocation toward calcium-magnesium precipitation functions.

During the continuous operation of the MICP reactor, *Halomonas* and *Corynebacterium* were consistently maintained at high relative abundances at the genus level, yet their functional contributions diverged significantly (Fig. 7 f). *Halomonas*, the core MICP genus, drove carbonate precipitation by highly expressing urease to catalyze urea hydrolysis [53,54]. In contrast, *Corynebacterium* could accelerate the CO_2 hydration reaction via secretion of carbonic anhydrase, thereby supplying additional CO_3^{2-} for precipitation, indicating metabolic complementarity between the two genera [55]. During Period I, the decline in the abundance of *Marinicella* (from 2.80 % to 2.40 %) weakened its synergistic interactions with *Halomonas*, disrupting substrate exchange and quorum-signaling networks [56]. This breakdown of critical cooperative networks likely contributed to the collapse of Ca^{2+} and Mg^{2+} precipitation. *Glycocaulis* could adapt to the high salt alkaline environment of HPW and exhibited a decline in relative abundance during the system collapse phase but gradually recovered in Period II [57]. Concurrently, *Tissierella* (a genus with MICP functionality) demonstrated a pronounced increase in relative abundance from 0.03 % to 2.75 % through functional microbial recruitment, transitioning from a rare taxon to a dominant genus [58]. This type of community succession indicates that the functional recovery of the MICP system relies not only on the persistence of environmentally adapted strains but also critically on niche replacement by taxa harboring key metabolic functions. Meanwhile, halophilic heterotrophic taxa including *Stappia*, *unclassified_f_-Flavobacteriaceae*, *SM1A02*, and *Marinobacterium* demonstrated chemoorganoheterotrophic metabolic potential and transmembrane nutrient transport functions. These taxa exhibited alkane and polycyclic aromatic hydrocarbon degradation capabilities, enabling efficient utilization of organics in HPW. Based on the Zi-Pi microbial co-occurrence network analysis framework, key species and functional modules in the MICP process were identified (Fig. 7e). The results demonstrated a significant increase in connector node quantities from 8 in Period I to 19 in Period II, indicating substantial expansion of ecological niches in core microbial taxa endowed with cross-module regulatory functions. *Halomonas* and *Pseudonocardia* were identified as core connector genera. KEGG-EC functional annotation confirmed their genetic encoding of complete urease gene clusters (ureA, ureB, ureC, and urease accessory protein) and EPS synthesis genes (Fig. 7h). These findings elucidated the microbiome transition from functional redundancy to the establishment of MICP-functional core microbiota. Enzymatic abundance prediction further detected urea transporter (utp) and Mg^{2+} transporter (mgTE), suggesting intracellular mineralization pathways involving Ca^{2+}/Mg^{2+} conversion to ACC or AMC. Elevated gene abundance of alkane monooxygenase and aldehyde dehydrogenase corroborated bacterial metabolic utilization of recalcitrant organics (e.g., long-chain hydrocarbons) present in HPW to sustain growth. Microbiome successfully overcame multiple stressors including high salinity, extreme hardness, and complex organic loads through metabolic complementarity and coordinated gene module expression.

4. Conclusions

In response to the complex pollution characteristics of heavy oil produced water, this study develops a MICP continuous operation technology system. For the first time, a targeted regulation method was reported for constructing an engineering microbiome through substrate gradient exposure acclimation, successfully achieving mineralization of hardness ions and degradation of organics in HPW. Providing a low carbon and efficient microbial mineralization strategy for produced water treatment in the petroleum industry. At the molecular scale, this work proposes a dual-pathway mineralization model dominated by extracellular heterogeneous nucleation and regulated by intracellular amorphous carbonate formation. Precisely identified the accumulation and crystallization hot-zone of Ca^{2+} and Mg^{2+}. This work advances the theoretical understanding of microbially mediated mineralization and provides practical significance for the integrated treatment of produced water.

Environmental implication

Heavy oil produced water (HPW), a by-product of unconventional oilfield development, is characterized by high salinity, extreme hardness, and complex organics, posing incalculable risks to the hydrosphere. Effective treatment of HPW is therefore essential for mitigating energy–water conflicts, while hardness ion removal further contributes to streamlining the recovery of valuable metals. This study constructed an engineering microbiome for stable hardness ions precipitation in HPW and revealed mineralization mechanisms under high salinity, offering a sustainable model for produced water green remediation.

CRediT authorship contribution statement

Jianhua Lei: Writing – review & editing, Writing – original draft, Supervision, Software, Methodology, Formal analysis, Data curation, Conceptualization. **Weizhi Zhou:** Writing – review & editing, Supervision, Methodology, Funding acquisition, Conceptualization. **Lei Zhang:** Visualization, Validation. **Yuke Li:** Validation, Investigation. **Shuhui Zhang:** Supervision, Software, Data curation. **Chuanfu Zhao:** Writing – review & editing, Investigation.

Declaration of Competing Interest

The authors declare no competing financial interest. The authors declare that they have no competing financial interests or personal relationships that could have appeared to influence the work reported in this paper.

Acknowledgements

This work was supported by National Key Research and Development Program (2022YFC2807503); Major Program of Shandong Province Technological Innovation Project (2020CXGC011403); National Natural Science Foundation of China (U1906221).

Appendix A. Supporting information

Supplementary data associated with this article can be found in the online version at doi:10.1016/j.jhazmat.2025.140317.

Data availability

Data will be made available on request.

References

[1] Wang, H., Lu, L., Chen, X., Bian, Y., Ren, Z.J., 2019. Geochemical and microbial characterizations of flowback and produced water in three shale oil and gas plays in the central and western United States. Water Res 164, 114942. https://doi.org/10.1016/j.watres.2019.114942.

[2] Yao, Y., Sun, D., Xu, J.-H., Wang, B., Peng, G., Sun, B., 2023. Evaluation of enhanced oil recovery methods for mature continental heavy oil fields in China based on geology, technology and sustainability criteria. Energy 278, 127962. https://doi.org/10.1016/j.energy.2023.127962.

[3] Cooper, C.M., McCall, J., Stokes, S.C., McKay, C., Bentley, M.J., Rosenblum, J.S., et al., 2022. Oil and gas produced water reuse: opportunities, treatment needs, and challenges. ACS EST Eng 2, 347–366. https://doi.org/10.1021/acsestengg.1c00248.

[4] Zhang, L., Mishra, D., Zhang, K., Perdicakis, B., Pernitsky, D., Lu, Q., 2021. Impact of influent deviations on polymer coagulant dose in warm lime softening of synthetic SAGD produced water. Water Res 200, 117202. https://doi.org/10.1016/j.watres.2021.117202.

[5] Fakhru'l-Razi, A., Pendashteh, A., Abdullah, L.C., Biak, D.R.A., Madaeni, S.S., Abidin, Z.Z., 2009. Review of technologies for oil and gas produced water treatment. J Hazard Mater 170, 530–551. https://doi.org/10.1016/j.jhazmat.2009.05.044.

[6] Feng, H., Lai, Y., Wang, X., Zhang, Z., Chen, S., 2025. Greater environmental risk of shale gas produced water from lacustrine than marine sources in Fuling shale gas field, China: insights from inorganic compounds, dissolved organic matter, and halogenated organic compounds. Water Res 268, 122719. https://doi.org/10.1016/j.watres.2024.122719.

[7] Shih, J.-S., Saiers, J.E., Anisfeld, S.C., Chu, Z., Muehlenbachs, L.A., Olmstead, S.M., 2015. Characterization and analysis of liquid waste from marcellus shale gas development. Environ Sci Technol 49, 9557–9565. https://doi.org/10.1021/acs.est.5b01780.

[8] Gallegos, T.J., Doolan, C., Caldwell, R., Engle, M.A., Varonka, M., Birdwell, J., et al., 2021. Insights on geochemical, isotopic, and volumetric compositions of produced water from hydraulically fractured williston basin oil wells. Environ Sci Technol. https://doi.org/10.1021/acs.est.0c06789.

[9] Chang, H., Lu, M., Zhu, Y., Zhang, Z., Zhou, Z., Liang, Y., et al., 2022. Consideration of potential technologies for ammonia removal and recovery from produced water. Environ Sci Technol 56, 3305–3308. https://doi.org/10.1021/acs.est.1c08517.

[10] Shaffer, D.L., Arias Chavez, L.H., Ben-Sasson, M., Romero-Vargas Castrillón, S., Yip, N.Y., Elimelech, M., 2013. Desalination and reuse of high-salinity shale gas produced water: drivers, technologies, and future directions. Environ Sci Technol 47, 9569–9583. https://doi.org/10.1021/es401966e.

[11] Mohanakrishna, G., Al-Raoush, R.I., Abu-Reesh, I.M., 2021. Integrating electrochemical and bioelectrochemical systems for energetically sustainable treatment of produced water. Fuel 285, 119104. https://doi.org/10.1016/j.fuel.2020.119104.

[12] Khoi, T.M., Tran, N.A.T., Jung, H.B., Huynh, V.P., Kim, Y., Hong, J., et al., 2023. Selective and continuous ion recovery using flow electrode capacitive deionization with polymer multilayers functionalized ion exchange membrane. Desalination 558, 116626. https://doi.org/10.1016/j.desal.2023.116626.

[13] Carrero-Parreño, A., Onishi, V.C., Ruiz-Femenia, R., Salcedo-Díaz, R., Caballero, J. A., Reyes-Labarta, J.A., 2019. Optimization of multistage membrane distillation system for treating shale gas produced water. Desalination 460, 15–27. https://doi.org/10.1016/j.desal.2019.03.002.

[14] Maltos, R.A., Regnery, J., Almaraz, N., Fox, S., Schutter, M., Cath, T.J., et al., 2018. Produced water impact on membrane integrity during extended pilot testing of forward osmosis – reverse osmosis treatment. Desalination 440, 99–110. https://doi.org/10.1016/j.desal.2018.02.029.

[15] Kondaveeti, S., Govindarajan, D., Mohanakrishna, G., Thatikayala, D., Abu-Reesh, I.M., Min, B., et al., 2023. Sustainable bioelectrochemical systems for bioenergy generation via waste treatment from petroleum industries. Fuel 331, 125632. https://doi.org/10.1016/j.fuel.2022.125632.

[16] Hu, L., Wang, H., Xu, P., Zhang, Y., 2021. Biomineralization of hypersaline produced water using microbially induced calcite precipitation. Water Res 190, 116753. https://doi.org/10.1016/j.watres.2020.116753.

[17] Rajasekar, A., Wilkinson, S., Moy, C.K.S., 2021. MICP as a potential sustainable technique to treat or entrap contaminants in the natural environment: a review. Environ Sci Ecotechnol 6, 100096. https://doi.org/10.1016/j.ese.2021.100096.

[18] Carter, M.S., Tuttle, M.J., Mancini, J.A., Martineau, R., Hung, C.-S., Gupta, M.K., 2023. Microbially induced calcium carbonate precipitation by sporosarcina pasteurii: a case study in optimizing biological $CaCO_3$ precipitation. Appl Environ Microbiol. https://doi.org/10.1128/aem.01794-22.

[19] Zhou, Y., Elchalakani, M., Cheng, L., Shahin, M.A., 2024. Impact of calcium content and pH value on MICP crack healing of geopolymer concrete. Cem Concr Comp 146, 105410. https://doi.org/10.1016/j.cemconcomp.2023.105410.

[20] Zhang, M., Wei, B., Liu, H., Liu, D., Gadd, G.M., Li, Q., et al., 2025. Simultaneous removal of hardness and organic matter from oilfield-produced water by microbially induced calcite precipitation. Water Res 276, 123252. https://doi.org/10.1016/j.watres.2025.123252.

[21] Li, L., Sun, H., Ren, C., Zhao, Z., Song, Y., Wang, M., et al., 2025. Synchronous removal of heavy metals and ammonia-nitrogen by magnesium ammonium phosphate (MAP)-enhanced microbial induced calcite precipitation (MICP). J Hazard Mater 498, 139994. https://doi.org/10.1016/j.jhazmat.2025.139994.

[22] Huang, H., Jia, M., Peng, D., Zhang, Y., Zheng, X., Li, Y., et al., 2025. Polyethylene microplastics interfere with MICP-based cadmium remediation: a dual-system evaluation of microbial performance and environmental response. J Hazard Mater 497, 139541. https://doi.org/10.1016/j.jhazmat.2025.139541.

[23] Yang, Z., Liu, L., Dong, Y., Gao, Z., 2024. Comparative study on the effect of SRB and *Sporosarcina pasteurii* on the MICP cementation and solidification of lead–zinc tailings. Chem Eng J 495, 153446. https://doi.org/10.1016/j.cej.2024.153446.

[24] Zhao, C., Lei, J., Han, F., Jiao, T., Han, Y., Zhou, W., 2023. Novel strategy for treating high salinity oilfield produced water: pyrite-activated peroxymonosulfate coupled with heterotrophic ammonia assimilation. Water Res 247, 120772. https://doi.org/10.1016/j.watres.2023.120772.

[25] Ghafoori, S., Omar, M., Koutahzadeh, N., Zendehboudi, S., Malhas, R.N., Mohamed, M., et al., 2022. New advancements, challenges, and future needs on treatment of oilfield produced water: a state-of-the-art review. Sep Purif Technol 289, 120652. https://doi.org/10.1016/j.seppur.2022.120652.

[26] Lei, J., Zhao, C., Zhang, S., Zhang, W., Han, Y., Zhou, W., 2024. New insight in the biotreatment of produced water: pre-oxidation paves a rapid pathway for substrate selection in microbial community. J Hazard Mater 480, 136483. https://doi.org/10.1016/j.jhazmat.2024.136483.

[27] Lawson, C.E., Harcombe, W.R., Hatzenpichler, R., Lindemann, S.R., Löffler, F.E., O'Malley, M.A., et al., 2019. Common principles and best practices for engineering microbiomes. Nat Rev Microbiol 17, 725–741. https://doi.org/10.1038/s41579-019-0255-9.

[28] Liu, Y., Ali, A., Su, J.-F., Li, K., Hu, R.-Z., Wang, Z., 2023. Microbial-induced calcium carbonate precipitation: influencing factors, nucleation pathways, and application in waste water remediation. Sci Total Environ 860, 160439. https://doi.org/10.1016/j.scitotenv.2022.160439.

[29] Blondeau, M., Sachse, M., Boulogne, C., Gillet, C., Guigner, J.-M., Skouri-Panet, F., et al., 2018. Amorphous calcium carbonate granules form within an intracellular compartment in calcifying cyanobacteria. Front Microbiol 9. https://doi.org/10.3389/fmicb.2018.01768.

[30] Qin, W., Wang, C., Ma, Y., Shen, M., Li, J., Jiao, K., et al., 2020. Microbe-mediated extracellular and intracellular mineralization: environmental, industrial, and biotechnological applications. Adv Mater 32, 1907833. https://doi.org/10.1002/adma.201907833.

[31] Yan, H., Zhu, X., Liu, Z., Jin, S., Liu, J., Han, Z., et al., 2024. Co-removal and recycling of Ba^{2+} and Ca^{2+} in hypersaline wastewater based on the microbially induced carbonate precipitation technique: overlooked Ba^{2+} in extracellular and intracellular vaterite. J Hazard Mater 475, 134923. https://doi.org/10.1016/j.jhazmat.2024.134923.

[32] Cong, M., Liu, Q., Wang, D., Hao, S., Han, Z., Xu, H., et al., 2024. Electrocatalytic urea synthesis from CO_2 and nitrate co-reduction on natural vitamin B_{12} coupled carbon nanotubes. Appl Catal B Environ 351, 123941. https://doi.org/10.1016/j.apcatb.2024.123941.

[33] Yu, J., Xiao, K., Xu, H., Li, Y., Xue, Q., Xue, W., et al., 2023. Spectroscopic fingerprints profiling the polysaccharide/protein/humic architecture of stratified extracellular polymeric substances (EPS) in activated sludge. Water Res 235, 119866. https://doi.org/10.1016/j.watres.2023.119866.

[34] Peschke, Michael, Blades, Arthur T., Kebarle, P., 2000. Binding energies for doubly-charged ions $M^{2+} = Mg^{2+}$, Ca^{2+} and Zn^{2+} with the Ligands L = H_2O, acetone and N-methylacetamide in complexes M for n = 1–7 from gas phase equilibria determinations and theoretical calculations. J Am Chem Soc 122 (42), 10440–10449. ⟨https://pubs.acs.org/doi/full/10.1021/ja002021z⟩, 2000.

[35] Hao, L., Yu, T., Liu, C., You, J., Guo, R., 2024. Modulation of electron transfer behavior on Fe_2P-Co_2P/NPC oxygen electrocatalyst by lattice cation substitution engineering and charge transport network design for rechargeable Zn-air batteries. Energy Storage Mater 72, 103723. https://doi.org/10.1016/j.ensm.2024.103723.

[36] Jin, B., Wang, S., Lei, Y., Jia, H., Niu, Q., Dapaah, M.F., et al., 2024. Green and effective remediation of heavy metals contaminated water using $CaCO_3$ vaterite synthesized through biomineralization. J Environ Manag 353, 120136. https://doi.org/10.1016/j.jenvman.2024.120136.

[37] Lee A.C., Park S.Y., Kim J.-H. Estimation of Mg/Ca Ratios in Biogenic Mg-Calcites in Methane-Derived Authigenic Carbonate From the Ulleung Basin, Korea, Using Raman Spectroscopy. J Raman Spectrosc https://doi.org/10.1002/jrs.6822.

[38] Feng, C., Zhao, S., Zong, Y., He, Q., Winarto, W., Zhang, W., et al., 2022. Microdroplet-based in situ characterization of the dynamic evolution of amorphous calcium carbonate during microbially induced calcium carbonate precipitation. Environ Sci Technol 56, 11017–11026. https://doi.org/10.1021/acs.est.1c08858.

[39] Yang, K., Zhang, Y., Dong, Y., Peng, J., Kaal, J., Li, W., et al., 2021. Tracking variations in the abundance and composition of dissolved organic matter in solar ponds of oilfield-produced brine. Appl Geochem 131, 105008. https://doi.org/10.1016/j.apgeochem.2021.105008.

[40] Wu, W., Lu, Z., Lu, C., Sun, X., Ni, B., Cölfen, H., et al., 2023. Bioinspired stabilization of amorphous calcium carbonate by carboxylated nanocellulose enables mechanically robust, healable, and sensing biocomposites. ACS Nano 17, 6664–6674. https://doi.org/10.1021/acsnano.2c12385.

[41] Pan, J., Zhang, S., Qiu, X., Ding, L., Liang, X., Guo, X., 2024. Molecular weights of dissolved organic matter significantly affect photoaging of microplastics. Environ Sci Technol 58, 13973–13985. https://doi.org/10.1021/acs.est.4c04608.

[42] Bala, T., Prasad, B.L.V., Sastry, M., Kahaly, M.U., Waghmare, U.V., 2007. Interaction of different metal ions with carboxylic acid group: a quantitative study. J Phys Chem A 111, 6183–6190. https://doi.org/10.1021/jp067906x.

[43] Han, Y., Zhang, W., Lei, J., Fei, X., Zhou, W., 2025. Surface hydroxyls of spinel oxides: a double-edged sword in the peroxymonosulfate activation process. Appl Catal B Environ 364, 124849. https://doi.org/10.1016/j.apcatb.2024.124849.

[44] Hao, X., Gao, S., Tian, J., Sun, Y., Cui, F., Tang, C.Y., 2019. Calcium-carboxyl intrabridging during interfacial polymerization: a novel strategy to improve

antifouling performance of thin film composite membranes. Environ Sci Technol 53, 4371–4379. https://doi.org/10.1021/acs.est.8b05690.
[45] Hu, X., Yu, C., Shi, J., He, B., Wang, X., Ma, Z., 2024. Biomineralization mechanism and remediation of Cu, Pb and Zn by indigenous ureolytic bacteria *B. intermedia* TSBOI. J Clean Prod 436, 140508. https://doi.org/10.1016/j.jclepro.2023.140508.
[46] Liu, B., Tang, C.-S., Pan, X.-H., Zhu, C., Cheng, Y.-J., Xu, J.-J., et al., 2021. Potential drought mitigation through microbial induced calcite precipitation-MICP. Water Resour Res 57, e2020WR029434. https://doi.org/10.1029/2020WR029434.
[47] Vaskevicius, L., Malunavicius, V., Jankunec, M., Lastauskiene, E., Talaikis, M., Mikoliunaite, L., et al., 2023. Insights in MICP dynamics in urease-positive *Staphylococcus* sp. H6 and *Sporosarcina pasteurii* bacterium. Environ Res 234, 116588. https://doi.org/10.1016/j.envres.2023.116588.
[48] Huang, H., Liao, J., Zheng, X., Chen, Y., Ren, H., 2019. Low-level free nitrous acid efficiently inhibits the conjugative transfer of antibiotic resistance by altering intracellular ions and disabling transfer apparatus. Water Res 158, 383–391. https://doi.org/10.1016/j.watres.2019.04.046.
[49] Yang, L., Zhou, J., She, Q., Wan, M.P., Wang, R., Chang, V.W.-C., et al., 2017. Role of calcium ions on the removal of haloacetic acids from swimming pool water by nanofiltration: mechanisms and implications. Water Res 110, 332–341. https://doi.org/10.1016/j.watres.2016.11.040.
[50] Huang, Y.-C., Rao, A., Huang, S.-J., Chang, C.-Y., Drechsler, M., Knaus, J., et al., 2021. Uncovering the role of bicarbonate in calcium carbonate formation at near-neutral pH. Angew Chem Int Ed 60, 16707–16713. https://doi.org/10.1002/anie.202104002.
[51] Toyofuku, M., Nomura, N., Eberl, L., 2019. Types and origins of bacterial membrane vesicles. Nat Rev Microbiol 17, 13–24. https://doi.org/10.1038/s41579-018-0112-2.
[52] Nicholas, T.C., Stones, A.E., Patel, A., Michel, F.M., Reeder, R.J., Aarts, D.G.A.L., et al., 2024. Geometrically frustrated interactions drive structural complexity in amorphous calcium carbonate. Nat Chem 16, 36–41. https://doi.org/10.1038/s41557-023-01339-2.
[53] Arias, D., Cisternas, L.A., Rivas, M., 2017. Biomineralization of calcium and magnesium crystals from seawater by halotolerant bacteria isolated from Atacama Salar (Chile). Desalination 405, 1–9. https://doi.org/10.1016/j.desal.2016.11.027.
[54] Zhao, T.-L., Li, H., Huang, Y.-R., Yao, Q.-Z., Huang, Y., Zhou, G.-T., 2019. Microbial mineralization of struvite: salinity effect and its implication for phosphorus removal and recovery. Chem Eng J 358, 1324–1331. https://doi.org/10.1016/j.cej.2018.10.139.
[55] Sharma, T., Kumar, A., 2021. Efficient reduction of CO_2 using a novel carbonic anhydrase producing *Corynebacterium flavescens*. Environ Eng Res 26. https://doi.org/10.4491/eer.2020.191.
[56] Zhao, C., Zhang, W., Guo, Y., Zhang, M., Han, F., Lei, J., et al., 2025. Flocculent sludge outperforms filler biofilm for high salinity oilfield produced water treatment: performance, metabolic pathways, and microbial communities. J Hazard Mater 492, 138217. https://doi.org/10.1016/j.jhazmat.2025.138217.
[57] Lv, X.-L., Xie, B.-S., Cai, M., Geng, S., Tang, Y.-Q., Wang, Y.-N., et al., 2014. Glycocaulis albus sp. nov., a moderately halophilic dimorphic prosthecate bacterium isolated from petroleum-contaminated saline soil. Int J Syst Evol Micr 64, 3181–3187. https://doi.org/10.1099/ijs.0.063537-0.
[58] Ji, G., Huan, C., Zeng, Y., Lyu, Q., Du, Y., Liu, Y., et al., 2024. Microbiologically induced calcite precipitation (MICP) *in situ* remediated heavy metal contamination in sludge nutrient soil. J Hazard Mater 473, 134600. https://doi.org/10.1016/j.jhazmat.2024.134600.